Received: 25 September 2019 | Revised: 2 December 2019 | Accepted: 3 December 2019

DOI: 10.1002/cjce.23747

THE CANADIAN JOURNAL OF CHEMICAL ENGINEERING

Canadian Society for Chemical Engineering | *For Our Future*
Société canadienne de génie chimique | *Pour notre avenir*

MINI-REVIEW

Experimental methods in chemical engineering: X-ray diffraction spectroscopy—XRD

Hayat Khan[1] | **Aditya S. Yerramilli**[2] | **Adrien D'Oliveira**[1] | **Terry L. Alford**[2] | **Daria C. Boffito**[1] | **Gregory S. Patience**[1]

[1]Chemical Engineering, Polytechnique Montréal, Montréal, Québec, Canada

[2]School for Engineering of Matter, Transport and Energy, Arizona State University, Tempe, Arizona

Correspondence
Daria C. Boffito, Chemical Engineering, Polytechnique Montréal, C.P. 6079, Succ. "CV", Montréal, H3C 3A7 Québec, Canada.
Email: daria-camilla.boffito@polymtl.ca

Abstract

X-ray diffraction (XRD) analysis identifies the long-range order (ie, the structure) of crystalline materials and the short-range order of non-crystalline materials. From this information we deduce lattice constants and phases, average grain size, degree of crystallinity, and crystal defects. Advanced XRD provides information about strain, texture, crystalline symmetry, and electron density. When radiation impinges upon a solid, coherent scattering of the radiation by periodically spaced atoms results in scattered beams that produce spot patterns from single crystalline samples and ring patterns from polycrystalline samples. The pattern, intensities of the diffraction maxima (peaks or lines), and their position (Bragg angle θ or interplanar spacing d_{hkl}), correlate to a specific crystal structure. In 2016 and 2017 close to 100 000 articles mention XRD—more than any other analytical technique, and it was the top analytical technique of researchers that published in *Can. J. Chem. Eng.* A bibliographic analysis based on the Web of Science groups articles referring to XRD into five clusters: the largest cluster includes research on nanoparticles, thin films, and optical properties; composites, electro-chemistry, and synthesis are topics of the second largest cluster; crystal morphology and catalysis are next; photocatalysis and solar cells comprise the fourth largest cluster; and, waste water is among the topics of the cluster with the least number of occurrences. Researchers publishing in *Can. J. Chem. Eng.* focus most of the XRD analyses to characterize polymers, nanocomposite materials, and catalysts.

KEYWORDS

crystallinity, Debye-Scherrer method, limit of quantification, nanoparticle, XRD

1 | INTRODUCTION

The Debye and Scherrer method,[1] known as x-ray powder diffraction is a non-destructive, quick qualitative and quantitative analysis of pure and multi-component mixtures that requires minimal sample preparation. When an x-ray beam impinges upon crystalline material, diffraction patterns form that reflect its structural physico-chemical characteristics. According to Hull (1919),[2] "every crystalline substance gives a pattern; the same substance always gives the same pattern; and in a mixture of substances, each produces its pattern independently of the others." It identifies crystal structure, degree of crystallinity, crystallite size and atomic spacing, crystalline phase, transition and their quantitative proportion, microstructure, quantitative resolution of chemical

Characteristic	XRD	NMR	MS	IR
Sample form	Crystal	L, S	G, L, S	G, L, S
Destructive	No	No	Yes	No
Atomic type measured	All	Limited	All	All
Determines configuration	Yes	indirect	No	No
Resolves absolute structure	Yes	indirect	No	No
Establishes crystal structure	Yes	No	No	No
Sample preparation	Easy	Middle	Easy	Easy
Data interpretation	Direct	Indirect	Indirect	Indirect

TABLE 1 Comparing XRD with other analytical techniques; G = gas, L = liquid, S = solid

species, isomorphous substitutions, unknown crystalline materials, and solids.[3] X-ray diffraction patterns are like fingerprints that identify crystalline samples by matching the pattern with the Joint Committee on Powder Diffraction Standards library (JCPDS).[4] Since it produces independent patterns of components in mixtures, it is a prevalent analytical technique in forensics, nanomaterials, catalysis, and geochemical materials. In 2016 and 2017, 90 articles in *Can. J. Chem. Eng*. mention XRD to characterize polymers,[5,6] composite materials,[7,8] catalysts,[9–11] membranes,[12–14] minerals,[15,16] and medicinal drugs,[17] which makes it one of the most used spectrometries.

In the early 20th century, physicists developed single crystal x-ray diffraction (SCXRD) to derive crystal and molecular structures and they were frequently awarded Nobel prizes—Laue (1914), Bragg and Bragg (1915), Siegbhan (1924), Debye (1936 - chemistry), and Davisson and Thomson (1937). While nuclear magnetic resonance (NMR), mass spectrometry (MS), and infrared spectroscopy (IR) are more suited for liquids and gases (and solids in the case of NMR), XRD resolves crystal structure directly (Table 1).

2 | THEORY

Crystalline materials have three dimensional regularity of atoms that form a crystal structure; based on one of the 14 Bravais lattices. When a monochromatic X-ray beam impinges onto the surface of a material, the atoms interact with the radiation to transmit, refract, scatter, and absorb it.[18,19] Unlike raindrops in the sky that diffract light to form a rainbow, diffraction requires coherent scattering of the radiation by the solid.[4] In this unique form of elastic scattering, there is no change in the energy of the x-ray after scattering.

Coherent scattering of radiation occurs due to the dimensional regularity of unit cells. The directions of the scattered beam depend on the interatomic spacing (d_{hkl}) of the plane and the radiation wavelength. The intensity of the scattered beam depends on the orientation of the crystal relative to the direction of the incident x-ray and the position of each atom inside the unit cells. Two ways in which the waveforms overlap in scattering are the constructive and destructive manner resulting in allowed reflections with non-zero intensity and disallowed reflections with minimal intensity. Diffraction criteria require the wavelength of the incident radiation, λ, to be smaller than the distance between scattering sites and that the scattering occurs in a coherent manner. Given that the atomic spacing is in the order of lattice constants (0.2 nm to 0.4 nm), radiation with a wavelength smaller than 0.2 nm is required to meet diffraction criteria. Only x-rays and high energy electrons meet this range of wavelength. For coherent scattering, the energy of the incident radiation should be equal to the energy of the scattered radiation.

One of, if not the simplest of x-ray analyses for powders uses a sealed cathode ray tube. An applied voltage of 10 kV to 60 kV across a hot filament accelerates electrons towards a metal anode (eg, Cu, Cr, Fe, Co, Mo, or Ag). Electrons decelerating produce white or background x-ray radiation.[3] When the bias is such that an electron removes an electron from a specific energy level, an electron from a specific high level transitions down to that shell and emits a characteristic x-ray. The emission only occurs if the electron level involved satisfies the Dipole Selections Rule 9.[4]

The binding energies of the electrons involved in the electronic transition define the x-ray wavelength. For example, in Cu, an electronic transition of an electron from the L_3 subshell to K subshell results in Kα_1 radiation. The energy of the emitted radiation is the difference in the binding energies. For Cu Kα_1 radiation, ΔE is the difference in the K-subshell binding energy (8.98 keV) and L_3 binding energy (0.94 keV) and equals 8.04 keV. This energy corresponds to a monochromatic beam of 0.1541 nm radiation. Typically, the Cu anode in a sealed tube emits the Cu Kα1 and Cu Kα2 and Cu Kβ. A

monochromator allows only the Kα_1 to pass. The Soller slits produce a narrow band of wavelengths of collimated x-rays, λ and directs it to the sample (Figure 1). The sample diffracts the radiation at angles that obeys Bragg's Law[18]:

$$n\lambda = 2d\sin\theta \quad (1)$$

where n is an integer (1, 2, 3, 4,...), d_{hlk} marks the interplanar spacing generating the diffraction, and θ is the x-ray incident angle.

This law accounts for the relationship between the wavelength of the produced electromagnetic radiation to the lattice spacing of the crystalline sample and diffraction angle. The radiation diffracts at discrete directions in space and an area detector or film records the reflections as the x-ray source completes an arc over the sample. The position and intensity of the reflection relate to the identity and position of the atoms in the unit cell[20] (Figure 2).

Powder x-ray diffraction has a wider applicability compared to single crystal analysis (SCXRD), but peaks overlap substantially more in the diffractogram compared to SCXRD of multicomponent samples, which obscures the position and intensities of the diffraction maxima (Figure 3, Table 2).[22,23] In powder XRD, a large number of individual crystallites intercept the incident x-rays and the individual beams of intensity become cones; the detector individual spots generate rings of varying intensity. We compare the peak intensity and d-spacing against the JCPDS library to identify crystals.

The mass fraction of each phase, X_i, in the mixture is based on the Zhang and Benfield equation that considers the peak intensity, I_i, and a coefficient derived for each component, k_i ($k_A = 0.884$, $k_B = 2.721$, $k_R = 1$)[24]:

$$X_A = \frac{k_A I_A}{k_A I_A + k_B I_A + I_R} = 0.81, \quad \text{anatase} \quad (2)$$

This approach requires that the component has the essential absorption coefficient when a standard is unavailable:

$$X_B = \frac{k_B I_B}{k_A I_A + k_B I_A + I_R} = 0.14, \quad \text{brookite} \quad (3)$$

$$X_R = \frac{I_R}{k_A I_A + k_B I_A + I_R} = 0.05, \quad \text{rutile} \quad (4)$$

Although the peak intensity of the anatase is almost 20× higher than rutile, its mass fraction is only 6× higher. The peak intensities correlate with composition, the peak position identifies the phase, unit cell parameters, group spacing, stress-strain analysis, and crystal system. The software completes the find and match procedure and identifies crystallographic planes—([101],

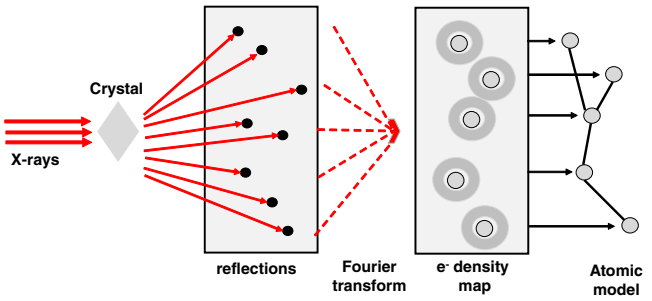

FIGURE 2 Single crystal XRD reflections.[21] A crystal diffracts an x-ray beam and a film or electronic detector record reflections on a 2-D surface. A Fourier transform of the pattern and intensity of the reflections produces an electron density map from which we derive an atomic model

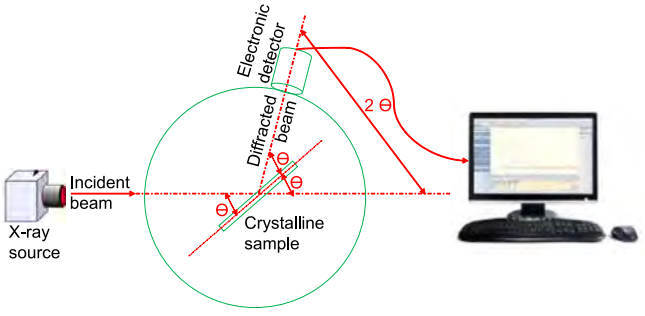

FIGURE 1 XRD instrument schematic. An incident x-ray beam shines on the surface and a film or electronic detector captures the signal as it completes an arc

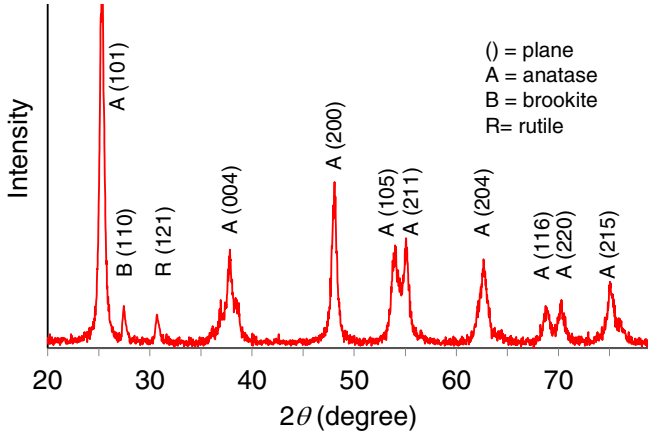

FIGURE 3 XRD diffractogram of TiO_2

TABLE 2 TiO_2 crystallographic parameters derived from the x-ray diffractogram (Figure 3). We assign the peak with the highest intensity 1000 and other peak heights are ratios of this value

Peak	Phase	2θ	Intensity	FWHM[a]
1	Anatase	25.3	1000	0.4133
2	Rutile	27.4	67	0.3542
3	Brookite	30.8	55	0.4723
4	Anatase	37.7	186	0.2952
5	Anatase	48	288	0.2952
6	Anatase	53.8	191	0.4723
7	Anatase	55	188	0.4132
8	Anatase	62.6	136	0.4723
9	Anatase	68.6	77	0.7084
10	Anatase	70.2	74	0.2362
11	Anatase	74	118	0.3542

[a]Full width at half maximum.

for example). The peak width (FWHM: full width at half maximum) correlates with crystal size, lattice distortion, and structural dislocation. The Williamson-Hill plot of $\beta\cos\theta/\lambda$ vs $\sin\theta$ gives a straight line with the slope equal to η/λ and the intercept is $1/d_p$:

$$\frac{\beta\cos\theta}{\lambda} = \frac{1}{d_p} + \frac{\eta\sin\theta}{\lambda} \tag{5}$$

where β= FWHM (in radians), d_p is the effective crystallite size, and η is the effective strain. We derive the crystallite size from Scherrer's equation:

$$d_p = \frac{0.9\lambda}{\beta\cos\theta} \tag{6}$$

The anatase crystallite size (Figure 3) is 20 nm, which is a little smaller than the rutile (23 nm) but larger that the brookite (17 nm) based on a copper metal target with $\lambda = 0.15418$ nm.

Under reaction conditions, catalysts calcine and become more crystalline, which increases the d_p and thereby the intensity as the peaks become narrower (Figure 4).[25,26] In situ XRD measures changes in catalyst and other materials structure during synthesis and reaction to identify structural changes associated with phase transition and chemical reactions Figure 5.

It has become straightforward to follow changes as a function of temperature, pressure, and gaseous environment while maintaining the signal quality throughout the duration of the test.[27,28] The following example shows the usefulness of the powder diffractometer with a hot stage that allows for in-situ heating and controlled ambient. In this case, we anneal a thin bilayer of Al (≈10 nm) and Ag (≈200 nm) that resides on a SiO_2 in an oxygen environment (for safety, Ar is the carrier gas).

At the onset of annealing, Al diffuses into the Ag to form a solid-solution that changes the lattice constant (Figure 6) At 725°C, the Ag peak gradually shifts to the original direction but less at 500°C. This confirms that the high temperature anneal accelerates Al diffusion through Ag films. Also, the (111) peaks are stronger at 725°C than 500°C at all time periods, which confirms that a higher temperature enhances the texture of Ag films.[29]

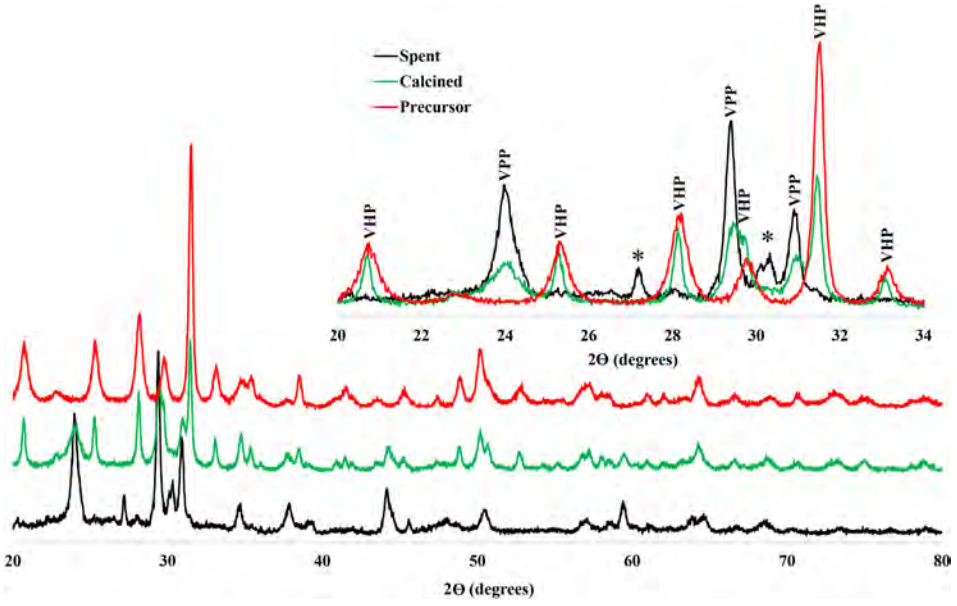

FIGURE 4 XRD diffractograms of vanadyl hemihydrate (precursor), calcined vanadium pyrophosphate (VPP), and equilibrated VPP after over 12 000 hours of continuous operation at 400°C[25,26]

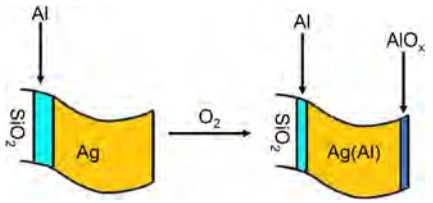

FIGURE 5 Al/Ag bilayer on a SiO_2 substrate

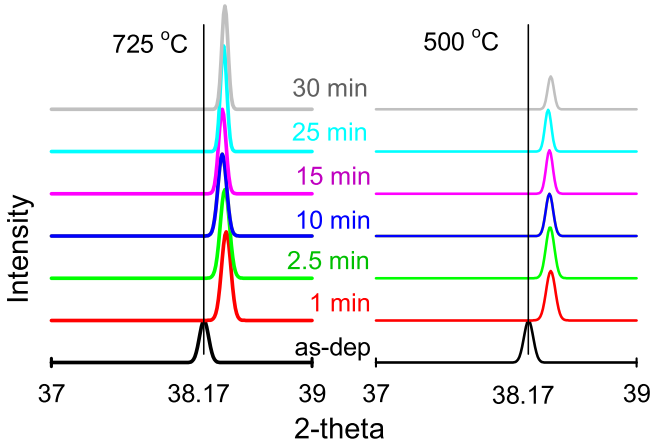

FIGURE 6 XRD: Ag (111) peak shifts as a function of anneal time at 725°C and 500°C

Synchrotron radiation, generated as charged particles accelerate in a straight-line path or travelling in a curved path, is extremely bright and monochromatic and produces diffractograms with minimal peak overlap. Electrons enter a storage ring several kilometers in circumference at high vacuum (10 to 12 Torr) to minimize particle loss by collision with residual gas atoms. In the storage ring, a magnetic field changes the direction of the high speed electrons so they emit electromagnetic radiation because of the angular acceleration—synchrotron radiation (SR)—that ranges from from microwaves ($\lambda > 1$ m) to hard x-rays (0.05 nm).[30] A synchrotron beam line incorporates collimating mirrors (collimates the beam in vertical direction into parallel light to improve the energy resolution[31]), slits, focusing mirrors, and Si (111) or germanium (220) double crystal monochromators to create tunable monochromatic x-rays and focus the beam in a horizontal direction.[32] The characteristics of synchrotron radiation that make it suitable for XRD include[33]: (a) bright x-rays that are 100× to 1000× more intense than conventional laboratory analyzers; (b) highly collimated beams to increase resolution; (c) a wide energy spectrum; and (d) a short pulsed time structure. These characteristics yield high signal/noise ratios and high angular resolution, while minimizing

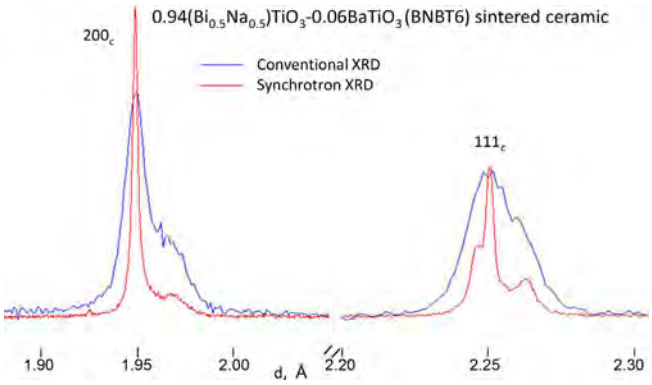

FIGURE 7 Synchrotron XRD diffractograms of sintered BNBT6 bulk ceramic compared with conventional XRD: conventional Cu-cathode x-ray tube (step 0.05 2θ and 5 seconds counting time) and synchrotron radiation at MCX beamline Elettra Sincrotrone, Trieste (step 0.005 2θ and 2 seconds counting time). Peaks are at least 10% narrower with the synchrotron XRD[34]

peak overlap and improving peak positioning (Figure 7). Furthermore, the $K_{\alpha 2}$ and K_{β} diffraction peaks are absent.

3 | APPLICATIONS

Researchers apply x-ray diffraction across a wide range of materials in dozens of scientific fields (Figure 8): metals and alloys, clays and minerals, catalysts, cement, ceramics, plastics, composites, corrosion products, fly ash, asbestos, solar cells, films, and semiconductors. Carbon-based materials—graphene, diamond, carbon nanotubes, carbon nanobuds, carbon nanofoams, and activated carbon—are finding application in sensors, optoelectronics, green adsorbents for pollutants, and electrochemical catalysts.[3] These novel materials require electron microscopy (SEM/TEM/EDX) to image local features at the nanometric scale and XRD to characterize the bulk characteristics because of its simplicity and reliability. While the applications in geology, building materials, and textiles examine strength, texture, and susceptibility to structural cracking, in forensic sciences, chemistry, and biology, researchers examine the microstructure and determine the stereochemistry to evaluate crystallinity and identify phase composition. In pharmaceuticals, it identifies polymorphs to design drugs.[35]

A bibliometric analysis of the top 10 000 cited articles in WoS (2016-2107) mentioning XRD grouped research into five clusters.[36,37] Nanoparticles is the most cited research topic associated with XRD (red cluster in Figure 9)—15% of the articles mention this keyword. Thin films, optical, and mechanical properties are the other frequent keywords in this cluster that includes 34 of the 107 most often cited keywords. Nanocomposites

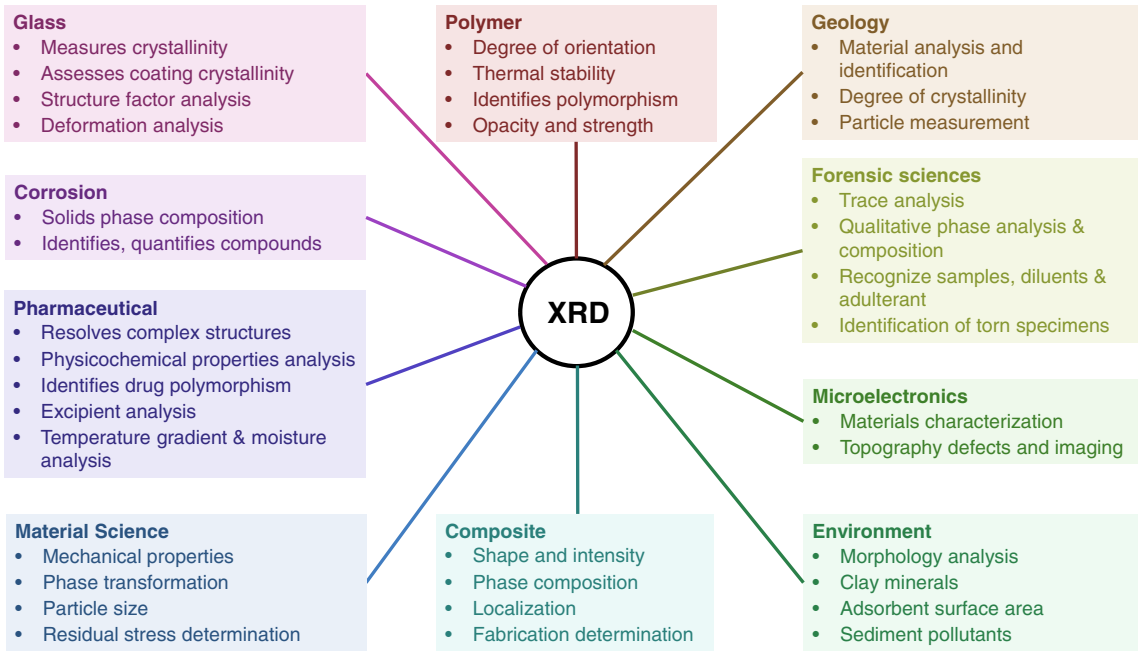

FIGURE 8 XRD applied in 10 fields of science

and composites figure prominently in the green cluster that comprises graphene, facile and hydrothermal synthesis, nanosheets, and battery type applications. Many of the subjects in the blue cluster relate to catalysis and include oxidation, reduction, crystal structure, and metal organic frameworks. The blue and green clusters comprise at least 25 keywords, while the yellow cluster and magenta cluster have 13 and 9 keywords, respectively. The major topics in the yellow cluster relate to photocatalysis and the environment, which includes TiO_2, degradation, and water. The subjects in the magenta cluster deal with waste water, adsorption, aqueous solutions, and activated carbon. WoS assigns the journals that publish most of these articles to categories related to chemistry: 3051 articles in physical chemistry, 2881 in multidisciplinary materials science, 1497 in multidisciplinary chemistry, 1225 in applied physics, and 1214 in chemical engineering. These categories are among the categories most related to chemical engineering.[38]

As of 2018, *Science Advances*, *Parasitology Research*, *Chemical Reviews*, and *Advanced Energy Materials* published the most cited articles with 680, 262, 218, and 163 citations, respectively. The top cited article, "Efficient luminescent solar cells based on tailored mixed-cation perovskites," synthesized a metal halide perovskite photovoltaic cell.[39] This work belongs mostly to the red cluster. The other three articles are all reviews, which are more often cited than original contributions.[40]

The review entitled "Plant-mediated biosynthesis of nanoparticles as an emerging tool against mosquitoes of medical and veterinary importance: A review" also belongs to the red cluster, as it describes how effective Ag nanoparticles are as ovicides, larvicides, pupicides, adulticides, and oviposition deterrents.[41] It mentions UV/vis spectroscopy, scanning electron microscopy, transmission electron microscopy, energy dispersive x-ray photoelectron spectroscopy, and Fourier transform infrared spectroscopy to characterize the nano-particles. *Discotic Liquid Crystals* cites 675 articles and describes advances in liquid crystals applied to anisotropic organic semiconductors in organic field effect transistors, organic light emitting diodes, and organic photovoltaic devices and includes basic structures, charge transport properties, and the classes of compounds for applications.[42] The third reveiw, "Recent Progress in Electrode Materials for Sodium-Ion Batteries" has keywords that fall in the green cluster, like lithium ion and energy storage.[43]

Energy & Environmental Science, *Chemical Engineering Journal*, and *Applied Catalysis B-Environmental* published the most cited articles in the chemical engineering category of WoS (145 citations in two-years). "Nickel selenide as a high-efficiency catalyst for oxygen evolution reaction" belongs to the green cluster (electrochemistry).[44] The second most cited chemical engineering article (141 citations) also belongs to the green cluster, as it considers electrochemical storage for supercapacitors: "Advanced electrochemical energy storage supercapacitors based on the flexible carbon fiber fabric-coated with uniform coral-like MnO_2 structured electrodes."[45] Solar cells (red cluster) and waste water

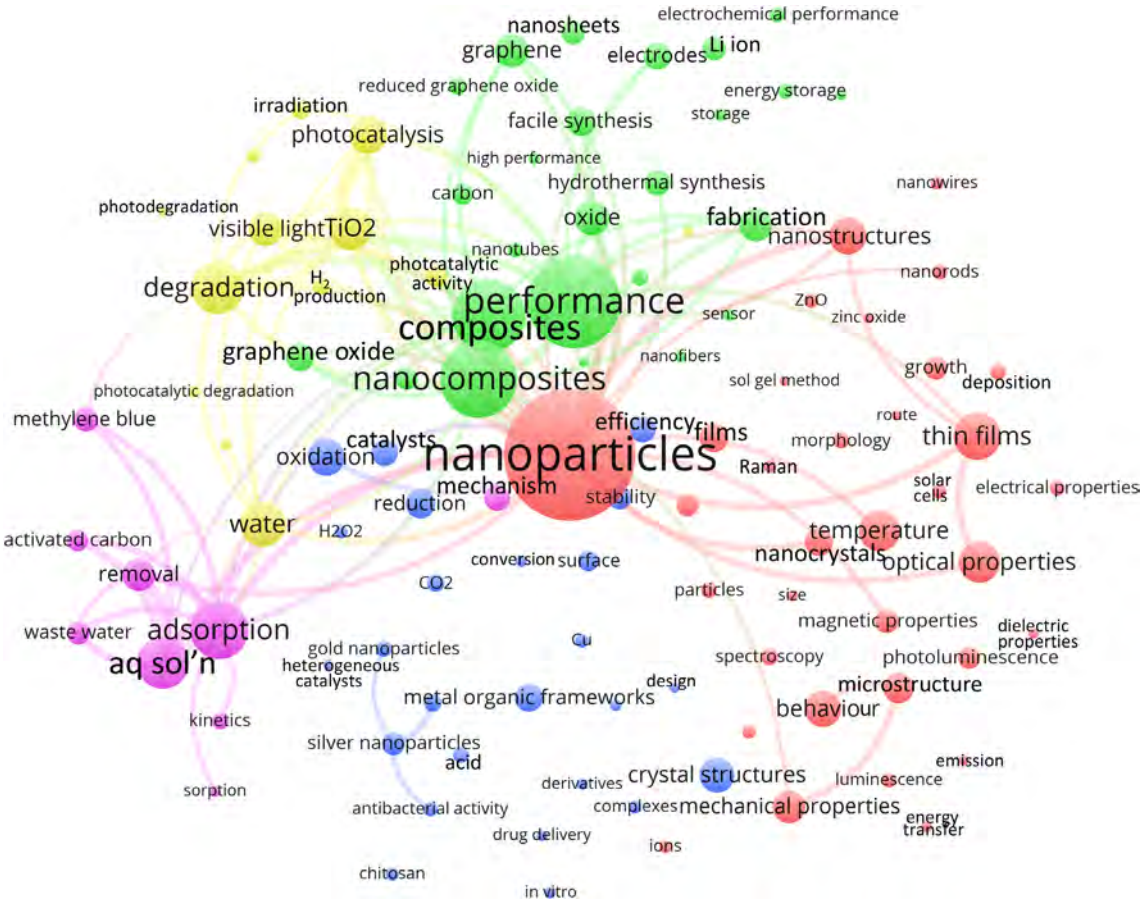

FIGURE 9 XRD bibliometric map generated by VOSviewer.[36,37] The data base consists of the top 107 keywords of the 10 000 most cited articles in WoS (2016-2017). The size of the circle represents the number of occurrences of the keyword in the 10 000 articles, while related research is grouped into clusters of the same colour. Nanoparticles appears in 1493 articles followed by performance (1054), oxidation (416), degradation (597), and adsorption (659). The least frequent of the top 100 keywords appear fewer than 130 times: sol gel method (117), supercapacitor (121), heterogeneous catalysts (115), sensitized solar cells (116), and sorption (126)

(magenta cluster) are the focus of the third and fourth most cited articles: "Structural and optical properties of methylammonium lead iodide across the tetragonal to cubic phase transition: implications for perovskite solar cells"[46] and "In situ synthesis of In2S3@MIL-125 (Ti) core-shell microparticle for the removal of tetracycline from wastewater by integrated adsorption and visible-light-driven photocatalysis,"[47] respectively.

4 | UNCERTAINTY

4.1 | Limitations

An XRD analyzer costs about 150 k$ and operating and maintenance costs are low with respect to other comparable analytical instruments. A complete analysis takes from 30 to 90 minutes. To produce a uniform and smooth surface, which is essential to maximize peak heights and minimize scattering, samples are pulverized. Poorly crystalline materials generate weak signals with broad diffraction peaks and a low intensity. For composite materials with standard analyzers, the detection limit is about 2%, but the sensitivity in a synchrotron is much better because of the greater precision of the beamline and higher energy.

4.2 | Sources of error

The major contributions to error of the peak analyses relate to sample type, instrument operation, and preparation.

4.2.1 | Sample related errors

1. Preferred orientation: To identify phases based on peak intensities requires a random orientation of the sample. Plates and crystallites have a preferred

orientation that introduces a systematic error in peak intensities. Standards are 100% crystalline to minimize order/disorder variability of amorphous materials.[48]

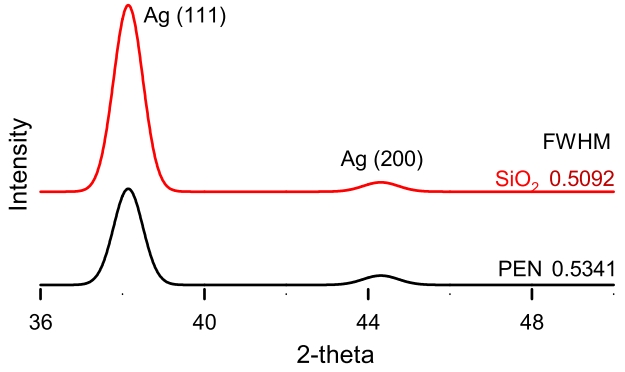

FIGURE 10 XRD scans ($\theta - 2\theta$) of Ag on SiO_2 and PEN substrates

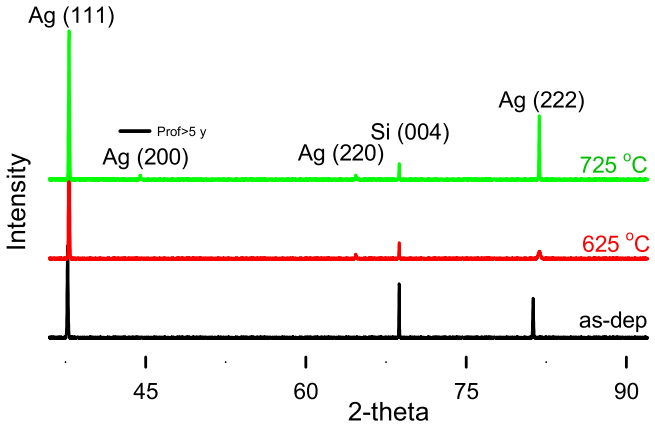

FIGURE 11 XRD data of encapsulated Ag layers annealed at 62°C and 725°C

Only the (111) and (200) reflections appear on the Ag thin film diffractograms over SiO_2 and the polymer substrate PEN (Figure 10). The major reflections of PEN substrates appear at 37° and 41° (Figure 10). Relative intensities of (200) that are normalized to the intensities of the (111) peak were calculated for Ag on SiO_2 as I200/I111 = 4.69 and PEN as I200/I111 = 13.19. These values indicated that Ag on SiO_2 has more (111) planes parallel to the surface than Ag on PEN. The full width at half maximum (FWHM) is inversely proportional to the grain size of the thin film. This implies that the average grain size of Ag on SiO_2 is higher than on PEN (Figure 10, $FWHM_{PEN} = 0.5341°$ and $FWHM_{SiO2} = 0.5092°$).

Figure 11 is another example of the preferred orientation during sample processing. X-ray diffraction spectra ($\theta - 2\theta$) of Ag (100 nm)/Al (30 nm) bi-layers annealed at 625°C and 725°C in NH_4 form an aluminium-encapsulation layer on the surface. The as-deposited sample shows a strong (111) texture that increases for the high temperatures anneal at 725°C.

2. Peak shape: Peaks of amorphous materials are typically broad and asymmetrical, which compromises quantifying how much is present.
3. Sample displacement: If the sample moves (dashed line above green block Figure 12A), the diffracted lines miss the detector aperature (solid lines vs dashed lines). As a result, the instrument incorrectly reports the peak position. The displacement error, *s*, is a function of the θ and the goniometer radius, *R*:

$$\Delta 2\theta = -\frac{2s\cos\theta}{R} \tag{7}$$

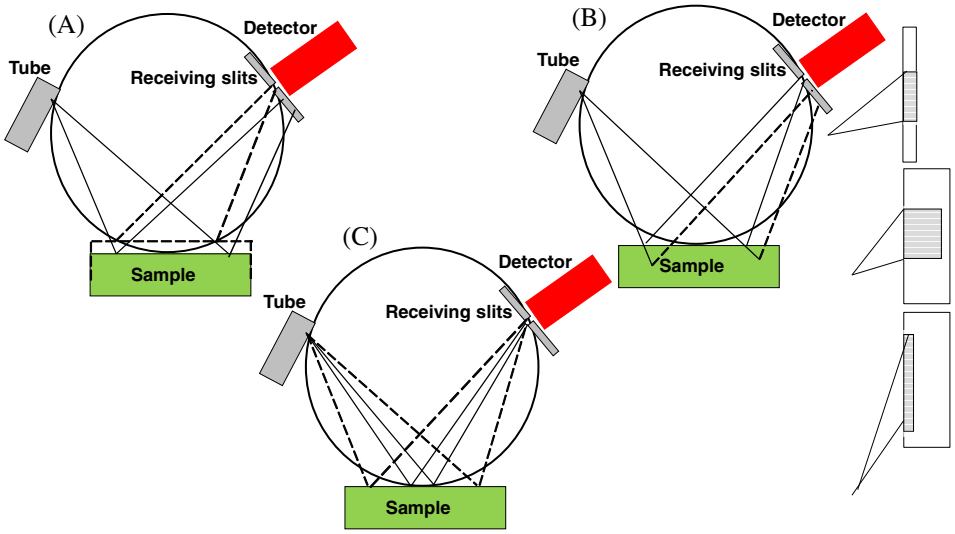

FIGURE 12 XRD instrument error: A, sample displacement error; B, sample transparency error; and, C, flat sample error

(in radians). For a displacement of $s = 0.15$ mm, the peak shift is 0.08° at $2\theta = 28.4°$ and $R = 200$ mm. Algorithms, which compensate for sample displacement errors, require internal calibration standards. Zero background sample holders and parallel-beam optics further minimize displacement errors.

4. Sample transparency error: X-ray penetration depth depends on the specimen mass absorption coefficient, μ, and the incident angle of the x-ray beam. Consequently, diffracted x-rays arrive from different points, (dotted lines vs solid lines in Figure 12B) and introduce peak position errors and peak asymmetry—the most common error for organic and low absorbing (low atomic number) specimens. Thin specimens and parallel beam optics minimize transparency error.
5. Plate sample error: When the entire surface of the flat sample cannot lie on the focusing circle (Figure 12C) the peaks are broader and asymmetric (at low 2θ angles). Narrow divergence slits with a shorter beam and parallel beam optics reduce this error.
6. Counting statistics: Statistical characterization of powders is best when the particle size is less than 10 μm. Diffractograms of large crystallite sizes and non-random orientations lead to peak intensity variations that are incongruent with an ideal powder (measured for many crystallites randomly oriented) and thus are poorly identifiable with reference patterns in the Powder Diffraction File (PDF) database.
7. Axial/vertical divergence error: Soller slits, capillary lenses, and decreasing the vertical opening of the counter slit maximize the diffracted intensity and reduce peak assymetric broadening due the divergence of the x-ray beam in the plane with the sample.[49]
8. Microabsorption: This error stems from differences in the interactions of each material with the x-ray beam, volume fractions of the components (large particles not crystallites), and on die geometrical peculiarities of their distribution.[50] Complex composites such as cements/concretes, coal combustion by-products (CCBs), and geologic materials are among the materials that are susceptible to microabsorption errors. Each material absorbs x-ray radiation depending on its linear absorption coefficient for the particular wavelength (energy). For example, CCBs have linear absorption coefficients ranging from 81 cm^{-1} for quartz to 1153 cm^{-1} for magnetite using copper radiation. Grinding and milling to a smaller particle size reduces this error.

4.2.2 | Instrumental errors

1. Sample fluorescence: Instrumental error is when incident x-ray radiation excites electrons of certain elements (V, Cr, Mn, Fe, Co, Ni, Cu, Zn, Ga). The excited electron emits a characteristic x-ray and the detector will record signals that are close to Cu Kα—increasing background noise but not position or intensity. Monochromators, β filters, energy sensitive detectors, and pulse height distribution levels (PHD) reduce the fluorescence contribution to the signal.
2. Equipment misalignment: The error of the "zero" 2θ position, ie, the offset of the instrument, introduces a systematic peak position error that is proportional to 2θ.[51] The source, sample, and detector must all be perfectly in line at 0° θ.

4.2.3 | Compositional variations errors

1. Grinding: Excessive grinding induces changes amorphism, strain, decomposition via local heating, and loss of volatile components. Some clays, zeolites, and engineered materials are sensitive to low-temperature damage. Shatter boxes or ball-mills produce a tail of very fine particles that broaden the diffraction peaks. Tungsten carbide and other brittle grinding media contaminate the sample and introduce additional peaks. Non-percussive techniques, like a mortar and pestle, reduce these errors.
2. Irradiation: Incident x-rays can interact with samples and change the composition, particularly for organic compounds. X-rays change the colour or cloud inorganic compounds without changing the diffractogram.
3. Environment: Elevated temperatures expand solids, inducing stress and strain. Water and other liquids interact with materials (clays and zeolite minerals, for example) and alter their structure.

4.3 | Detection limits

Following the rules of a Poisson distribution for N counts at 2θ, the absolute and relative SD σ and σ_{rel} are:

$$\sigma = \sqrt{X} \tag{8}$$

$$\sigma_{rel} = \frac{\sqrt{X}}{X} = \frac{1}{\sqrt{X}} \tag{9}$$

The limit of detection (LOD) of a particular reflection is:

$$X_{\text{reflection}} > X_{\text{background}} > 3\sigma_{\text{background}} \quad (10)$$

For example, measuring an $X_{\max}$ of 10 000 counts, the $\sigma_{\text{rel}} = 0.01$, corresponding to a relative error of 1%, the counting statistical error. (Note: Suppose we have a background of 100 counts and a small hump of 120 counts. This cannot be classified as a reflection for the reason that $3\sigma_{\text{background}} = 30$ is obviously higher than 20. The only solution is to increase the measurement time to improve the peak background ratio.)

4.4 | Limit of quantification

In the analysis of multiphase samples, an important consideration is the question of the lower limit of quantification (LOQ). What is the smallest amount of a given phase that can be identified by XRD? The LOQ depends on preferred orientation, matrix effect crystal symmetry, peak overlap, and amorphous content. Generally, the LOQ of a phase must be determined by a calibration curve.

Practitioners cite a lower limit of 5%, but this value varies with the composition of the constituents. Catalysts, for example, are often deposited on high surface area substrates to minimize the mass of costly metals. To demonstrate the effect of the substrate on the LOQ, we prepared five samples of Ru on TiO_2, activated carbon, and zeolite (ZSM-5). Ruthenium(III) chloride (45% to 55%) and activated charcoal (DARCO[textregistered]—100 mesh particle size, powder) were purchased from Sigma-Aldrich. ZSM-5 and ammonium (powder, S.A 400 $m^2\ g^{-1}$, 30:1 mol ratio SiO_2:Al_2O_3) were obtained from Alfa Aesar. Venator forwarded the titanium oxide (TP Hombikat, 100 μm).

We followed a wetness impregnation method in which we first added water to determine the total pore volume. We dissolved the ruthenium(III) chloride in the calculated volume. For a more intimate contact between the active phase and the catalyst, we mixed the liquid and the solid in a rotary evaporator for 3 hours at 70 rpm. After increasing the temperature by 5°C every 30 minutes until 85°C, we decreased the pressure to 300 mbar for 2 hours to dry the catalyst. A furnace calcined the solid: first it maintained the temperature constant at 120°C for 4 hours to remove traces of water followed by a 2.5°C min^{-1} ramp to 600°C, then a 4 hours hold in air.

To ensure that the Ru remained on the supports after synthesis, we measured the concentration with a SLOWPOKE nuclear reactor (Table 3). Nuclear bombardment detects all elements from F to higher molar mass (except Pb). For this reason, the analysis reports high mass fractions of Ru for the AC samples. Otherwise, agreement between the expected value based on the recipe agrees with that measured value by nuclear bombardment.

TABLE 3 Ru mass fraction on supports: The second column summarizes concentration based on the recipe and the third is based on nuclear activation analysis. The last column is the uncertainty in the nuclear activation. The Ru/AC concentration is high since the carbon is undetected

Catalyst	Wet deposition g g^{-1}, %	Nuclear g g^{-1}, %	Δ g g^{-1}, %
Ru/ZSM-5	1.5	1.38	0.06
Ru/AC	1.5	32.2	1.3
Ru /AC	3	46.2	1.8
Ru/TiO_2	5	4.76	0.19
Ru/TiO_2	1.5	2.01	0.08

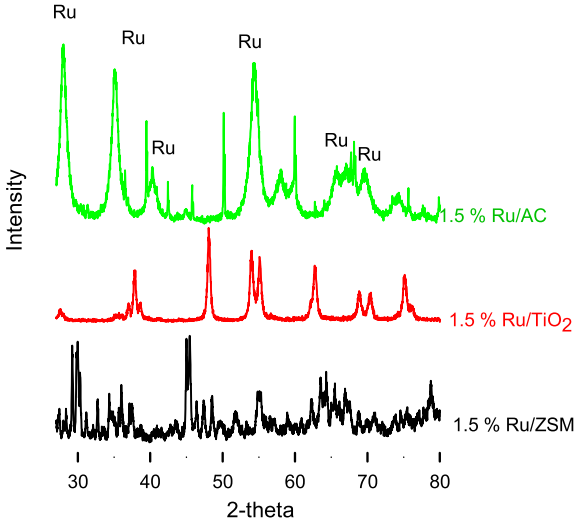

FIGURE 13 XRD diffractograms of 1.5% RuO_2 on activated carbon, TiO_2, and ZSM-5 supports

The minimum concentration that XRD detects depends on the nature of the support and distribution (Figure 13): a mass fraction of 1.5% RuO_2 on ZSM-5 is undetectable, while a slight shoulder is evident at 38° on the TiO_2 sample. TiO_2 has a very compact tetragonal crystalline structure and we expect to see more RuO_2 on the surface. The Ru shoulder on the TiO_2 is more evident for the sample with a mass fraction of 5% (Figure 14). The surface area of ZSM-5 is 240 $m^2\ g^{-1}$ so perhaps more of the Ru enters the structure.[52] AC is composed of carbon (graphite) layers of fused hexagons held by weak van de Waals forces and surface area can exceed 1000 $m^2\ g^{-1}$. Interestingly, XRD readily detects the 1.5% Ru and the peaks grow for the sample with a mass fraction of 3%

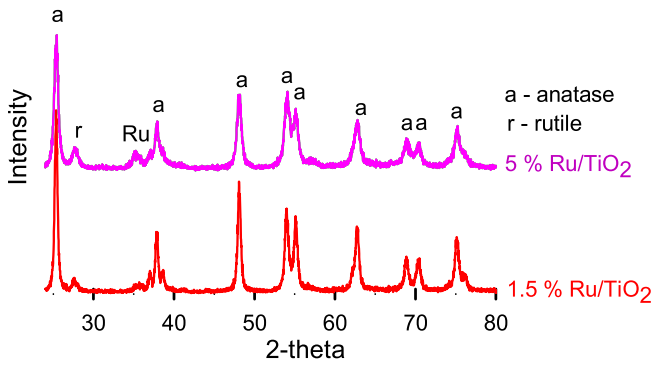

FIGURE 14 XRD diffractograms of RuO_2 on TiO_2. The intensity scale is identical to that of Figures 13 and 15

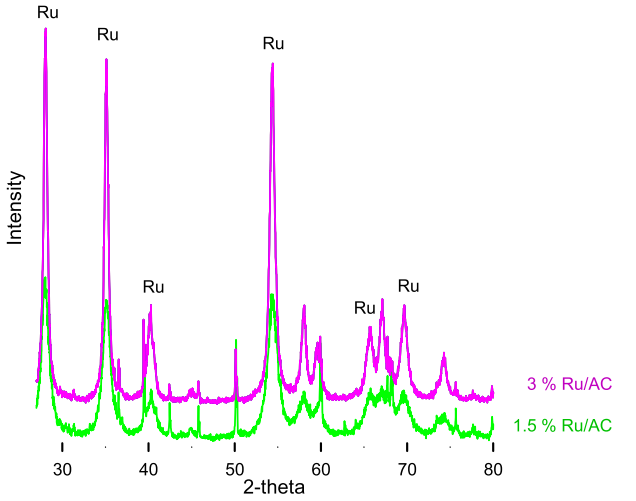

FIGURE 15 XRD diffractograms of RuO_2 on activated carbon. The intensity scale is identical to that of Figures 13 and 14

(Figure 15). At 2θ between 65° to 70° the two peaks are better resovled at a mass fraction of 3% compared to 1.5%. SEM-EDX analysis of these samples showed that the RuO_2 interacted little with the AC and rather formed large independent crystals. XRD analysis alone was incapable of differentiating between a species deposited on a support and the same species present as a segregated phase in the same sample. SEM-EDX analysis locates the different phase compositions in a small specimen and is complementary to XRD.

4.5 | Crystallinity

Sample crystallinity is the ratio of the total intensities in the diffraction pattern, N_{net}, and the sum of all the measured intensities, N_{tot}, including the amorphous part and air scatter, N_{scat}. The latter must be determined separately (measuring a zero background holder) and then subtracted:

$$C = 100\frac{\Sigma N_{net}}{\Sigma N_{tot} - \Sigma N_{scat}} \quad (11)$$

The ratio between the pure crystalline phase and the amorphous phase of the sample, C, depends on the peak position of each reflection in the mixture.

$$N(2\theta) = m[C \cdot N_c \cdot (2\theta) + (1-C) \cdot I_a \cdot 2\theta] \quad (12)$$

where $N(2\theta)$ is the intensity at (2θ) of the actual sample and of both the pure crystalline (c) sample, pure amorphous (a) sample, and the sample mass, m. The three diffractograms have to be corrected for air scattering by measuring a reference sample. The formula is valid for an amorphous material with the same elemental composition and the same density as the crystalline materials.

5 | SAFETY CONSIDERATIONS

XRD instruments are user friendly, however, x-rays are extremely hazardous so both trained personnel and occasional users must take the necessary precautions to avoid exposure to direct and secondary radiation. The effects of exposure to x-ray radiation are cumulative and cause serious and permanent injury—burns, for example. Frequent users should wear a dosimetry badge and check it and their blood to confirm that radiation exposure is negligible.[48]

6 | CONCLUSIONS

Availability and accuracy of XRD instrumentation and software has improved rapid analysis and characterization of composite materials. However, there remains room to advance the technology to overcome limitations with respect to time (analysis under 20 minutes), low sensitivity for hybrid materials, hybrid peaks at high angles, and a common control library of simulated diffraction patterns of various nanomaterials. Advances in software address some of these limitations to derive more from the wealth of information in XRD spectra. For example, big data tools could analyze collimated nanobeams that resolve crystals at the nanoscale with millisecond temporal resolution. Integrating XRD with SEM-EDX/TGA/DSC/FTIR/Raman instruments and microreactors expands its capability providing crystallographic data in situ that will also address issues in pharmaceuticals and other industries.

ACKNOWLEDGEMENTS

The authors gratefully acknowledge the assistance of Marco Rigamonti for the XRD diffractorgrams of the VPP and Brendan Patience for collecting the bibliometric data.

ORCID

Daria C. Boffito https://orcid.org/0000-0002-5252-5752
Gregory S. Patience https://orcid.org/0000-0001-6593-7986

REFERENCES

[1] P. Debye, P. Scherrer, *Z. Phys.* **1916**, *17*, 277.
[2] A. Hull, *J. Am. Chem. Soc.* **1919**, *41*, 1168.
[3] R. Das, E. M. Ali, S. B. A. Hamid, *Rev. Adv. Mater. Sci.* **2014**, *38*, 95.
[4] T. L. Alford, L. C. Feldman, J. W. Mayer, *Fundamentals of Nanoscale Film Analysis*, Springer, Boston **2007**.
[5] G. S. Patience, *Can. J. Chem. Eng.* **2018**, *96*, 2312.
[6] S. Strandman, R. Vachon, M. Dini, S. Giasson, X. Zhu, *Can. J. Chem. Eng.* **2018**, *96*, 20.
[7] C. Han, H. Liu, L. Zhang, J. Deng, Y. Luo, *Can. J. Chem. Eng.* **2017**, *95*, 543.
[8] F. Tari, M. Shekarriz, S. Zarrinpashne, A. Ruzbehani, *Can. J. Chem. Eng.* **2017**, *95*, 1632.
[9] Y. Dai, Z. Fei, X. Xu, X. Chen, J. Tang, M. Cui, X. Qiao, *Can. J. Chem. Eng.* **2016**, *94*, 1140.
[10] G. Fan, R. Lin, Z. Su, X. Lin, R. Xu, W. Chen, *Can. J. Chem. Eng.* **2017**, *95*, 717.
[11] H. Nguyen, T. Dang, N. Nguyen, H. Nguyen, N. Dinh, *Can. J. Chem. Eng.* **2018**, *96*, 832.
[12] J. Hu, X. Yang, J. Yu, G. Dai, *Can. J. Chem. Eng.* **2016**, *94*, 340.
[13] A. Farjoo, S. M. Kuznicki, *Can. J. Chem. Eng.* **2016**, *94*, 2219.
[14] S. Mondal, A. Elkamel, D. Reinalda, K. Wang, *Can. J. Chem. Eng.* **2017**, *95*, 1993.
[15] M. Geramian, D. Ivey, Q. Liu, T. Etsell, *Can. J. Chem. Eng.* **2018**, *96*, 49.
[16] R. Multani, K. Waters, *Can. J. Chem. Eng.* **2018**, *96*, 1185.
[17] M. A. Rahimi, A. S. A. Ramazani, H. A. Alijanvand, M. H. Ghazanfari, M. Ghanavati, *Can. J. Chem. Eng.* **2017**, *95*, 83.
[18] A. Bunaciu, E. Udristioiu, H. Aboul-Enein, *Crit. Rev. Anal. Chem.* **2015**, *45*, 289.
[19] G. S. Patience, *Experimental Methods and Instrumentation for Chemical Engineers*, 2nd ed., Elsevier, Amsterdam, the Netherlands **2017**.
[20] J. Evans, E. Radosavljevic, *Chem. Soc. Rev.* **2004**, *33*, 539.
[21] K. Hasegawa, *Rigaku J.* **2012**, *28*, 14.
[22] C. Tsuboi, F. Kimura, T. Tanaka, T. Kimura, *Cryst. Growth Des.* **2016**, *16*, 2810.
[23] D. Kenneth, E. Cheung, *Chem. Soc. Rev.* **2004**, *33*, 526.
[24] H. Zhang, J. Banfield, *J. Phys. Chem. B* **2000**, *104*, 3481.
[25] G. S. Patience, R. E. Bockrath, J. D. Sullivan, H. S. Horowitz, *Ind. Eng. Chem. Res.* **2010**, *46*, 4374.
[26] G. S. Patience, R. E. Bockrath, *Appl. Catal. A* **2010**, *376*, 4.
[27] K. Harris, M. Tremayne, B. Kariuki, *Angew. Chem. Int. Ed.* **2001**, *40*, 1626.
[28] B. Kariuki, K. Psallidas, K. Harris, R. Johnston, R. Lancaster, S. Staniforth, S. Cooper, *Chem. Commun.* **1999**, *17*, 1677.
[29] Y. Wang, *Ph.D. Thesis*, Arizona State University, Tempe, AZ, **2001**.
[30] Z. Dauter, *J. Mol. Struct.* **1996**, *374*, 29.
[31] M. Isshiki, Y. Ohishi, S. Goto, K. Takeshita, T. Ishikawa, *Nucl. Instrum. Methods Phys. Res.* **2001**, *467-468*, 663.
[32] T.-Y. Yang, W. Wen, G.-Z. Yin, X.-L. Li, M. Gao, Y.-L. Gu, L. Li, Y. Liu, H. Lin, X.-M. Zhang, B. Zhao, T.-K. Liu, Y.-G. Yang, Z. Li, X.-T. Zhou, X.-Y. Gao, *Nucl. Sci. Technol.* **2015**, *26*, 1.
[33] H. Cheng, C. Lu, J. Liu, Y. Yan, X. Han, H. Jin, Y. Wang, Y. Liu, C. Wu, *Prog. Nat. Sci.: Mater. Int.* **2017**, *27*, 66.
[34] E. Cobas, M. Cabrera, L. Pardo, L. Montero, *Materials* **2016**, *9*, 1.
[35] P. Fewster, *Acta Crystallogr., Sect. A: Found. Adv.* **2014**, *A70*, 257.
[36] Clarivate Analytics, *Web of Science Core Collection*, http://apps.webofknowledge.com (accessed: June 2018).
[37] N. J. van Eck, L. Waltman, *Scientometrics* **2010**, *84*, 523.
[38] G. S. Patience, C. A. Patience, F. Bertrand, *Can. J. Chem. Eng.* **2018**, *96*, 1684.
[39] D. Q. Bi, W. Tress, M. I. Dar, P. Gao, J. S. Luo, C. Renevier, K. Schenk, A. Abate, F. Giordano, J. P. C. Baena, J. D. Decoppet, S. M. Zakeeruddin, M. K. Nazeeruddin, M. Gratzel, A. Hagfeldt, *Sci. Adv.* **2016**, *2*, e1501170.
[40] G. S. Patience, C. A. Patience, D. C. Boffito, P. A. Patience, F. Bertrand, *Can. J. Chem. Eng.* **2016**, *94*, 805.
[41] G. Benelli, *Parasitol. Res.* **2016**, *115*, 23.
[42] T. Wohrle, I. Wurzbach, J. Kirres, A. Kostidou, N. Kapernaum, J. Litterscheidt, J. C. Haenle, P. Staffeld, A. Baro, F. Giesselmann, S. Laschat, *Chem. Rev.* **2016**, *116*, 1139.
[43] H. Kim, H. Kim, Z. Ding, M. H. Lee, K. Lim, G. Yoon, K. Kang, *Adv. Energy Mater.* **2016**, *6*, 1600943.
[44] A. T. Swesi, J. Masud, M. Nath, *Energy Environ. Sci.* **2016**, *9*, 1771.
[45] M. Cakici, K. R. Reddy, F. Alonso-Marroquin, *Chem. Eng. J.* **2016**, *309*, 151.
[46] C. Quarti, E. Mosconi, J. M. Ball, V. D'Innocenzo, C. Tao, S. Pathak, H. J. Snaith, A. Petrozza, F. D. Angelis, *Energy Environ. Sci.* **2016**, *9*, 155.
[47] H. Wang, X. Yuan, Y. Wu, G. Zeng, H. Dong, X. Chen, L. Leng, Z. Wu, L. Peng, *Appl. Catal. B* **2016**, *186*, 19.
[48] G. Garcia-Granada, J. Montejo-Bernardo, *X-Ray Diffraction—Powder, Reference Module in Chemistry Molecular Sciences and Chemical Engineering*, Elsevier, Amsterdam, the Netherlands **2013**.
[49] B. Cullity, S. Stock, *Elements of X-Ray Diffraction*, Pearson Education Limited, New Delhi **2014**.
[50] H. Hermann, M. Ermrich, *Powder Diffr.* **1989**, *4*, 189.
[51] M. F. de Campos, J. C. D. R. Machado, C. A. Achete, presented at Metrology for a Sustainable Development Brazil, XVIII IMEKO World Congress, Rio de Janeiro September **2006**.
[52] M. Menéndez, J. Herguido, A. Bérard, G. S. Patience, *Can. J. Chem. Eng.* **2019**, *97*, 2383.

How to cite this article: Khan H, Yerramilli AS, D'Oliveira A, Alford TL, Boffito DC, Patience GS. Experimental methods in chemical engineering: X-ray diffraction spectroscopy—XRD. *Can J Chem Eng*. 2020;98:1255–1266. https://doi.org/10.1002/cjce.23747